

Projected Ionospheric Location and Travel Time of Kelvin-Helmholtz Instabilities Occurring at the Low Latitude Boundary Layer

E. Hyatt, Undergraduate Student

Embry-Riddle Aeronautical University, Daytona Beach, FL 32114

Abstract. The Kelvin-Helmholtz Instabilities (KHI) are important in explaining solar wind transport from the magnetosheath to the magnetopause, particularly during northward IMF ((*Nykyri et al.* [2006], *Hasegawa et al.* [2004], *Otto et al.* [2000])). However, their identification by satellite observations can be challenging due to the vast size of the magnetosphere compared to the spacecraft coverage of the region. Determining a ground-based methodology of identification would therefore be an asset to the scientific community. To aid in this effort, the proper identification of an ionospheric signature is needed. This research is purposed to determine the ionospheric location of a KHI, the amount of time it would make for the instability to travel to the ionosphere, and the estimated area of the vorticity in the ionosphere. This would allow scientists to know when and where to look in the ground based data to document a potential KHI signature in the ionosphere.

1. Introduction

Kelvin-Helmholtz Instabilities (KHI) are a phenomenon present at a boundary involving the interaction between two fluids experiencing a shear flow involving different velocities. The onset condition for a KHI in magnetized plasma is given as (*Chandrasekhar* [1961])

$$[\mathbf{k} \cdot (\mathbf{V}_1 - \mathbf{V}_2)^2] > \frac{n_1 + n_2}{4\pi m_0 n_1 n_2} [(\mathbf{k} \cdot \mathbf{B}_1)^2 + (\mathbf{k} \cdot \mathbf{B}_2)^2]$$

where \mathbf{k} represents the direction of propagation of the shear flow plane, \mathbf{V} is the shear flow velocity in its given region, and \mathbf{B} is the magnetic field in its given region. The subindices refer to the different sides of the shear flow boundary. *Fairfield et al.* [2000] studied the evolution and signatures of KHI, showing they can cause mass transport, particularly during periods of strong northward IMF. Magnetohydrodynamic (MHD) simulations indicate reconnection can occur inside the current layers generated by KHI (*Fairfield et al.* [2000]), providing the major mass transport mechanism for the solar wind to enter into the magnetosphere (MSP) (*Nykyri et al.* [2001]). *Nykyri et al.* [2006] used satellite observations to confirmed reconnection inside the vortices,

showing reconnection can happen at two regions in the vorticity; at the boundary between anti-parallel magnetosheath (MSH) and MSP field, where the twisting of the boundary caused by the vorticity takes place and at the low density part of the wave in a layer of positive current. This reconnection can transport plasma which originated in the solar wind into the MSP. *Otto et al.* [2000] showed large and rapid magnetic field changes where the B_z component of the magnetic field would could assume an orientation not consistent with the field on both sides of the low-latitude boundary layer. The identification of these events using in-situ spacecraft observations is a challenging task, as the location of satellites at the MSP boundary at the exact moment of the instability is a rare occasion. In an effort aid to better help identify the KHI events, establishing signatures of the KHI in the ionosphere can allow scientists to identify the 'cause', the KHI, by observing the 'effect', the ionospheric signature. The motivation for this research falls under this broader effort. In order to recognize these potential signatures, known cases of KHI must be accurately mapped into the ionosphere and their ionospheric signatures observed by ground and in-situ spacecraft observations. This research aims to properly iden-

tify the correct ionospheric location and travel time of the magnetospheric perturbation into the ionosphere.

Past publications have hinted at possible ionospheric signatures of KHI events. These signatures were believed to be the effect of small scale field aligned currents which originated from the KHI vorticity. *Lui* [1989] observed images of auroral bright spots on the day-side oval from the Viking Imager. He believed KHI was the cause based on the time scales for the bright spot intensification and the lack of consistent direction of their motion. He measured the bright spots to be 50-200 km in diameter. *Farrugia et al.* [1994] observed optical auroral vorticies which was deduced to be cause by field aligned currents from KHI at the inner edge of the low-latitude boundary layer, viewing vorticies of 40-100 km in dimension. They documented rapidly evolving spiral forms centered on magnetic zenith which lasted for minutes and lacked a directed motion. They rule out other possibilities of creation, such as reconnection and magnetospheric compression, leaving KHI to be the probable generating source.

Model field line mapping capabilities provide an opportunity to map Earth's magnetic field lines from the observing satellite position to the ionosphere during the events unique magnetospheric environment. The NASA Community Coordinated Modeling Center (CCMC) hosts magnetospheric models which provide this ability. Their models produce output coordinates of the field line locations every few hundred kilometers, which also grants the ability to estimate the time of travel from the perturbation to the ionosphere.

Table 1 displays the KHI event list used for this project, populated from previously published observations of KHI, as well as events discovered by fellow Master's student Thomas Moore at Embry-Riddle Aeronautical University. All events were observed by the European Space Agency's Cluster satellite constellation. Shown are the date and times for each event, as well as their GSM and GSE coordinates in the MSP for Cluster spacecraft 1.

2. Methodology

2.1. Model Selection

CCMC has multiple MHD models for research, including four models which provide the field line tracing capability; Open Geospace General Circulation Model (OpenGGCM), Block-Adaptive-Tree-Solarwind-Roe-Upwind-Scheme (BATS-R-US), Global Solar Wind-Magnetosphere-Ionosphere coupling Model (GUMICS), and Lyon-Fedder-Mobarry (LFM). Event 3 from Ta-

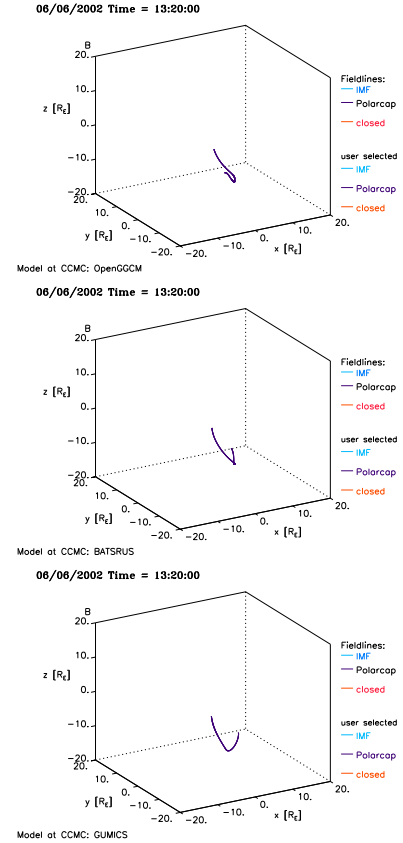


Figure 1. Mapped field lines of the Event 3 Cluster satellite formation at 13:20UT for each model. Reference Table 2 to determine the coordinate systems for each model figure.

ble 1 was chosen to run on all four models to show the difference in field line mapping outputs. Each model was ran with the same date and time.

Figure 1 displays three CCMC models' mapped field lines for Event 3 at the beginning of its event window, where each model name is listed below their plots. LFM is not shown, as it uses a different coordinate system than those provided by the Cluster satellite locations. As seen in Table 2, the models do not output coordinates in the same system. GUMICS and OpenGGCM used the same geocentric solar equatorial system (GSE) coordinate system, but the rest use solar magnetic (SM) and geocentric solar magnetic system (GSM). Even though the models have different coordinate systems for output, they all use the coordinates for the mapped field lines into the ionosphere, magnetic latitude and magnetic local time.

Event	Model	Time Window	Cluster [GSM, R_e]	Cluster [GSE, R_e]	References
1	07/03/2001	05:00-06:00	-8.87, -16.62, 4.11	-8.87, -16.93, 2.55	<i>Nykyri et al. [2006]</i>
2	11/20/2001	20:15-20:45	-3.66, 18.54, -2.63	-3.66, 18.67, -1.34	<i>Hasegawa et al. [2004]</i>
3	06/06/2002	13:20-13:50	-3.53, -16.11, -5.62	-3.53, -15.79, -6.47	T. Moore
4	06/13/2002	15:10-15:19	-5.27, 16.21, 5.40	-5.27, -16.04, -5.83	T. Moore
5	06/19/2004	08:58-09:22	-6.25, -17.70, -2.62	-6.25, -17.09, -5.34	T. Moore
6	06/19/2004	09:40-10:00	-6.35, -17.56, -2.76	-6.35, -16.84, -5.71	T. Moore
7	06/21/2004	03:40-04:00	-2.98, -16.25, 2.32	-2.98, -16.10, -3.17	T. Moore

Table 1. Event Dates and Times

	BATS-R-US	OpenGGCM	LFM	GUMICS
Dipole Update	Yes	No	Yes	No
B	1.18, -1.5, 0.54	1.18, -5.1, 0.54	0.1, -5.34, -0.09	0, -5.1, 0.54
V	-366.93, -14.17, -8.53	-366.93, -14.17, -8.53	-366.64, -14.67, -9.84	-366.93, -14.17, -8.53
N	4.28	4.28	4.12	4.28
T	19350.2	19350.2	19147.5	19350.2
Corotation	Real-time	No	Real-time	No
Coord. System	GSM	GSE	SM	GSE

Table 2. Average model input variables for Event 3

Table 2 lists some of the Advanced Composite Explorer (ACE) solar wind inputs and other model parameters required for each model to run. Some models handle their initial solar wind values differently. GUMICS does not allow for an averaged values for the B_x of the solar wind, but instead sets the solar wind B_x to zero. GUMICS therefore was ruled out to be less accurate, as the other models allowed for an ACE solar wind averaged B_x value to be used. Updating the dipole moment with time and using real-time corotation values were other parameters which varied per model.

After consulting with Dr. Masha Kuznetsova of CCMC, she recommended we use OpenGGCM and BATS-R-US for our research needs, eliminating LFM from the list. As LFM used a different coordinate system for its output, it would have been harder to visually compare mapped field lines of LFM versus any other model, and the Cluster satellites were not easily available for this coordinate system. There are minor differences in the results between OpenGGCM and BATS-R-US likely due to the updating of the dipole moment and the differences in their numerical scheme when solving the MHD equations. As both models output coordinates in different systems, all values shown in this paper will reflect the model's own coordinate system; GSM for BATS-R-US and GSE for OpenGGCM. BATS-R-US model solves the 3D MHD equations us-

ing a numerical scheme related to Roe's Approximation Riemann Solver (*NASA:CCMC*). It allows for a simulation parameter to be set to update the dipole moment with time and is solved on a finite volume adaptive grid (*NASA:CCMC*). OpenGGCM model solves the resistive MHD equations using second order explicit time integration with conservative and flux-limited spatial finite differences (*NASA:CCMC*). It does not update its dipole moment with time throughout the simulation. It also uses a stretched Cartesian grid and does not include energetic particle drifts and ring current physics (*NASA:CCMC*). As BATS-R-US has the ability to include a ring current model, we chose to exclude this physics to stay consistent with the abilities of OpenGGCM.

2.2. Choosing Model Times

A methodology was needed for how to pick a time in the event window during which we mapped the field lines from the satellite, as event time lengths varied. We used four minute data resolution in both MHD models. The user could choose which four minute time step to plot plasma and magnetic field parameters within the event time window. A test was ran to see how the using the start and end positions of the Cluster satellites with the start and end time of the event window would change the location of the mapped field lines. Three

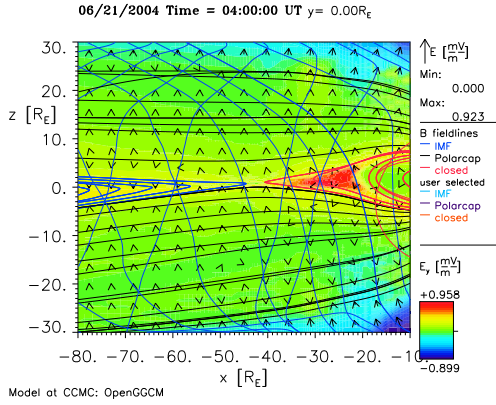


Figure 2. Event 7 tail-ward reconnection show in in OpenGGCM model at 04:00UT. The vector arrows and color bar represents E_y .

test cases were chosen from Table 1 to determine how significant the differences in mapped field line coordinates were during an entire event interval. Our test cases were Event 1, 3, and 7 with corresponding 60, 30, and 20 minute length time windows. Once the models were ran, the mapped field lines positions were noted for the start time of the event window with its corresponding satellite positions and the positions for the end of the event window with its corresponding satellite positions. The original thought was the change in mapped field line position would be a function of event duration; the longer the event window, the larger the mapped position change would be.

From observing the results in Table 3, it was clear that the difference in field line position was not based on event window length; There was a variety of position changes in different ionospheric coordinates for all three events. As this difference in position based on satellite location corresponding to the start and end time of the event window was not based on the duration of the interval, it was decided to gather the mapped ionospheric locations for all events using their start and end time satellite positions. A possible explanation for the significant position change even in the shorter event duration could be the magnetospheric tail or cusp dynamics. If reconnection in the tail or the cusp was occurring during the event time, the dynamics could largely effect the position of the field lines mapped to the Earth.

Figure 2 shows evidence of tail-ward reconnection in the OpenGGCM model for Event 4. The intense red color located near the last closed field line (red) indicates a large y-component of the electric field, E_y ,

which could have been produced from tail-ward reconnection. Upon looking at the field line topology during this event, this tail-ward reconnection did not effect the field lines the Cluster satellites were mapped into. Event 7 had the smallest difference in different event time window field line mapping, which is consistent with this finding. We took a look at the cusp for Event 3, which had the largest difference in field line mapping position. Reconnection was possible at the dayside cusp, as this event was during northward IMF with a negative B_y .

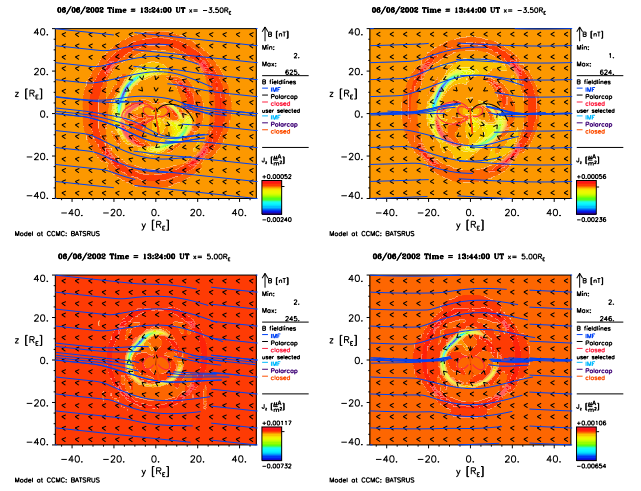


Figure 3. Change in mapped field line position possibly due to changing field line topology resulting in cusp reconnection for Event 3. Satellite coordinates can be referenced in Table 1.

Figure 3 shows how a difference in 20 minutes during reconnection can change the mapped magnetic field line when reconnection is occurring. The high y-component of the current density, J_y , is a signature of magnetic shear leading to magnetic reconnection. The top plots in the figure show the z-y plane at a $x = -3.5$ cut, corresponding to the satellite position for Event 3. The bottom plots in the figure show the z-y plane also, but at $x = 5$ cut plane, where the highest J_y value was found. You can see the magnitude of J_z in the plots is higher than the surrounding region. The satellites were located in this region, so the change in field line topology due to the cusp reconnection could explain the significant change in the mapped field line positions for Event 3. Event 1 also showed similar cusp reconnection signatures.

Event	Model	Time Window	MLAT _N	MLT _N	MLAT _S	MLT _S
1	BATS-R-US	Start	67.34	9.45	-65.01	2.91
1		End	68.34	9.84	-70.02	2.74
1	OpenGGCM	Start	65.29	8.48	-80.65	4.77
1		End	64.07	8.48	-72.54	3.72
3	BATS-R-US	Start	-	-	-63.56	1.14
3		End	-	-	-60.77	1.41
3	OpenGGCM	Start	-	-	-71.52	1.63
3		End	-	-	-74.59	1.00
7	BATS-R-US	Start	68.87	10.25	-76.48	2.70
7		End	66.88	10.23	-77.12	2.54
7	OpenGGCM	Start	67.00	11.24	-80.70	4.98
7		End	66.56	11.59	-81.69	5.00

Table 3. Mapped field line output difference for Event 1, 3 and 7 for each model based on varying the satellite positions as corresponding to the start and end of the event time window. These coordinates are for satellite 1.

2.3. Perturbation Travel Time

The simple concept of kinematics was used to determine the amount of time it would take for the perturbation originating from the magnetosphere to the ionosphere along magnetic field lines. Both CCMC models produced a list of set variables along the mapped field lines every few hundred kilometers, including the positions of the field lines in GSM coordinates and the magnetic field strength. The ending altitude for the time lag analysis was determined by the altitude limitation of the models' output files. The average ending altitude for all events ran using OpenGGCM was 3.7 R_e and 3.5 R_e for BATS-R-US, which is averaged to be 23,000 km. However, our altitude of interest in the ionosphere is 100 km. As auroral altitude is based on ionospheric conditions (*Deehr et al. [2005]*), an average of auroral altitude can be taken as 100 km. Convection vortices as seen by the Super Dual Auroral Radar Network (SuperDARN) reflect in the F-region (150-800 km) (*Greenwald et al. [1995]*), however as determined in Section 3.3, this altitude difference does not alter the travel time results significantly. There are heavier elements once we reach these lower altitudes, but we will neglect this as heavier elements such as O^+ as they are not abundantly present until the end of our desired altitude (*Finlay et al. [2010]*). Section 3.3 discusses the time contribution due to these changes in density and other factors. In order to calculate the time lag between KHI occurrence and a potential ionospheric signature, the Alfvén speed was calculated using the average magnetic field strength associated with a given field line position.

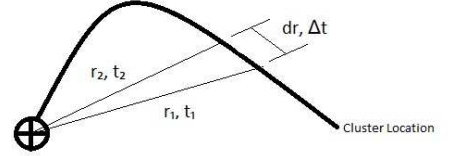


Figure 4. Illustration of methodology of calculating the perturbation travel time

$$dr = |\vec{r}_2 - \vec{r}_1| \quad V_{avg} = \frac{V_{a1} + V_{a2}}{2} \quad \delta t = \frac{dr}{V_{avg}}$$

where $V_a = \frac{B}{\sqrt{\mu\rho}}$. The difference in vector position of two field line positions was calculated. The Alfvén speed was averaged between two positions, then divided under dr to determine the length of time it took to travel from r_1 to r_2 . This calculation occurred at each location as listed by the CCMC model output, allowing the δt to be added together for each change in position to yield the total travel time from the satellite positions to the termination altitude of the model. This analysis was started at the exact, or nearest to the exact satellite coordinate for each satellite and each event.

3. Results

3.1. Field Line Mapping Results

The CCMC MHD models yielded field line mapping results to the Earth for all events except Event 2, for

Event	Time Window	MLAT _N	MLT _N	MLAT _S	MLT _S
1	start	67.35	9.43	-64.70	2.87
	end	68.38	9.82	-69.84	2.73
2	start	-	-	-	-
	end	-	-	-	-
3	start	-	-	-63.57	1.14
	end	-	-	-60.87	1.41
4	start	51.31	13.44	-	-
	end	-	-	-	-
5	start	59.05	10.72	-	-
	end	58.40	10.86	-	-
6	start	59.38	10.93	-	-
	end	59.01	10.67	-67.84	1.46
7	start	66.90	10.24	-76.41	2.71
	end	66.89	10.29	-77.10	2.55

Table 4. BATS-R-US magnetic latitude and local time (UT) coordinates for each pole.

Event	Time Window	MLAT _N	MLT _N	MLAT _S	MLT _S
1	start	65.42	8.45	-80.14	4.68
	end	64.09	8.48	-72.93	3.77
2	start	-	-	-	-
	end	-	-	-	-
3	start	-	-	-71.51	1.63
	end	-	-	-74.61	1.00
4	start	58.29	9.87	-	-
	end	58.27	9.91	-	-
5	start	58.43	1.48	-59.49	9.93
	end	58.28	1.64	-59.63	9.91
6	start	58.32	1.76	-59.94	9.82
	end	60.80	2.28	-59.84	9.91
7	start	67.06	11.23	-80.38	4.98
	end	66.56	11.58	-81.63	5.01

Table 5. OpenGGCM magnetic latitude and local time (UT) coordinates for each pole.

four satellites, at the start and end times of the event window.

As the goal was to compile a list of one field line mapped location per event, an average over the four positions at both ends of the time windows. The deviation in position was calculated based on the difference in ionospheric location of the field lines for both start and end satellite positions and is represented by the average deviation value seen in Table 6. This difference was averaged for both models per event for one satellite. Table 6 lists the location in magnetic latitude and local time (UT) at the end of the simulation ($\sim 3.6R_e$) for each event.

All KHI event dates, except Event 2, resulted in mapped field lines to at least one of the hemispheres. As the two models put out different locations, a test was ran to see if the position output of the mapped field lines was significant enough to contribute to the mapped location difference. Two test cases were ran on Event 1 and 3, to determine if there was a resolution difference in the models and if it would be significant enough to contribute to the difference in mapped field line position. These cases were chosen so the tests would include a field line which mapped to the north and south pole (Event 1) and a field line which mapped to one pole (Event 3) to see if there was a resolution dependency based on the type of mapped field line.

As shown in Table 7, BATS-R-US has a higher resolution than OpenGGCM does. This has been confirmed by CCMC, as BATS-R-US has a finer grid resolution than OpenGGCM. Event 1 has more resolution than Event 3, possibly due to the difference in mapped field line type. CCMC also confirmed this; field lines with both ends closed have more iteration steps than a field line with only one end closed.

3.2. Perturbation Travel Time Results

The difference in travel time duration between the four satellites for a given event was under one second on average, therefore the final travel time addition to one or both ionospheric positions was represented by the first satellite position.

Table 8 shows the travel time in seconds for each event and model. The additional time addition from the models' termination altitude of $\sim 3.6 R_e$ to our altitude of interest, 100 km, is discussed in Section 3.3. With the exception of Event 6, both models output times of travel into the ionosphere that are similar enough to understand.

Figure 5 shows how the difference in mapped field

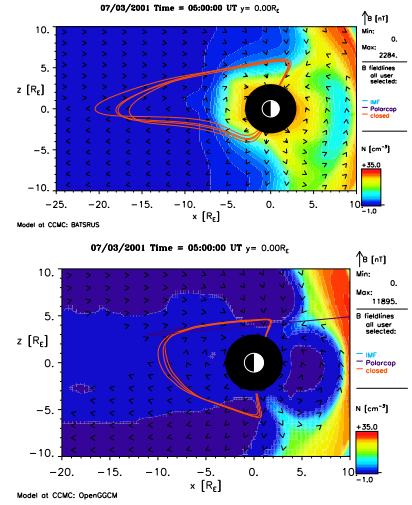


Figure 5. Difference in projected field lines for Event 1. The satellite coordinates at the start of the event are shown in Table 1. The left image were produced from BATS-R-US and the right was from OpenGGCM.

lines and can yield over a minute of difference in perturbation arrival time in the ionosphere. The noted exception, Event 6, gives us an example of an extreme case how the model's results vary significantly.

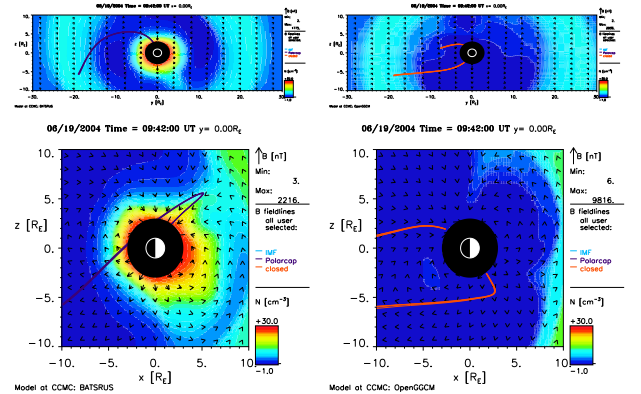


Figure 6. Difference in projected field lines for Event 6. The satellite coordinates at the start of the event can be referenced from Table 1. The left top and bottom images were produced from BATS-R-US and the two on the right were from OpenGGCM.

The difference between these events' travel times are due to the large difference in projected field lines, as we can see in plotted field lines of the two models in Figure 6. A main difference between the two models lies

Event	MLAT_N	MLT_N	MLAT_S	MLT_S
1	66.4	9.1	-71.9	3.5
2	-	-	-	-
3	-	-	-67.6	1.3
4	54.8	11.7	-	-
5	58.5	6.5	-59.6	9.9
6	58.9	6.4	-62.3	7.3
7	66.8	10.8	-78.9	3.8
Avg. Deviation	2.0	4.7	9.3	1.5

Table 6. Averaged magnetic latitude and local time (UT) coordinates for each event with corresponding deviation for each pole.

Model	Event 1 [R_e]	Event 3 [R_e]	Avg. [R_e]	Avg. [km]
BATS-R-US	0.010	0.066	0.053	338
OpenGGCM	0.006	0.055	0.030	191

Table 7. Difference in field line location steps for Event 1 and 3.

Event	t_N [sec]	t_S [sec]	t_N [sec]	t_S [sec]
	OpenGGCM		BATS-R-US	
1	213.2	300	103.6	566.3
2	-	-	-	-
3	-	105.4	-	170.4
4	108.3	-	70.8	-
5	892.1	60.7	181.3	-
6	1626.7	36.9	138.9	-
7	85.2	334.7	114.1	325.2

Table 8. Travel time in seconds for each event and model to reach $\sim 3.6R_e$ for each pole.

Event	t_N [m]	t_S [m]
1	2.6	7.2
2	-	-
3	-	2.3
4	1.5	-
5	15.1	1.0
6	8.6	0.6
7	1.7	5.5

Table 9. Average travel time in minutes for each event to reach $3.6 R_e$ for each pole.

within ones ability to update the dipole moment with each numerical iteration. Different numerical analysis techniques could also produce different results. It is also interested to note that Event 5, which occurs only 20 minutes before Event 6, has a shorter travel time to the north pole in the OpenGGCM model.

Table 9 shows the approximate average travel times from the initial location of the KHI event to $\sim 3.6 R_e$ which will be used to add on to the event time windows when looking at ground satellite data. Using these times will provide us with the most accurate time for when a signature can be expected in the data.

3.3. Change in Alfvén Speed at the Magnetosphere-Ionosphere Transition

To produce the most accurate travel time results, all variable changes which effect the Alfvén speed must be taken into account. We looked at the effect of increasing magnetic field strength and density as our altitude dropped towards Earth and the projected end-of-model altitude travel time to our altitude of interest. Our altitude of interest is 100 km, where aurora commonly occurs (*Deehr et al.* [2005]). Convection vortices occur in the F-region (150-800 km) (*Greenwald et al.* [1995]), however as seen in Table 10, the time travel difference in the aurora and convection vorticity altitudes is negligible. Event 1 and 3 were once used again as test cases.

Figure 7 shows the change in density for O^+ over an altitude from 2,500-100 km provided by the Ionospheric Reference Ionosphere (IRI) Model (*Bilitza* [2001]). The model was ran for both dates with time tags at the beginning of their events at their projected magnetic location on the Earth. Numerous ion density's were acquired from the model, however oxygen held the most prominent ion in altitudes above 100 km. As seen in Figure 7, the percentage of oxygen ions can depend on date, time, and location.

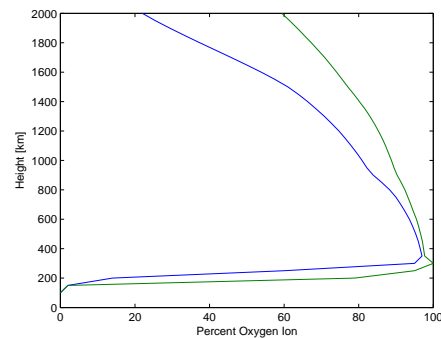


Figure 7. O^+ percentage in the atmosphere per height. The blue line represents Event 1, red line represents Event 3 at their event start times.

As seen in Table 10, there are multiple methods of how to determine additional travel time from our model termination altitude to our altitude of interest. Method 1 used a time projection from the ending altitude of the CCMC model's, $3.6 R_e$ to 2,500 km was determined using the V_a of the last calculated B as determined by the CCMC model variables. The distance was assumed to be a straight line resulting in an added 1.15 seconds to the travel time. To calculate the most extreme result, the travel time was calculated from the average height of significant O^+ population, 2,500 km to 100 km assuming a 100% population of the ion (*Bilitza* [2001]). V_a from the end of the CCMC model was divided by the square root of oxygen's mass number, to account for the $\rho^{1/2}$ in the Alfvén speed calculation. This over-estimation of density change resulted in an add of 1.08 seconds to the travel time. Method 1 would therefore add 2.23 seconds to the times listed in Table 9.

Next, a similar change in variables calculated was performed for the change in B strength with altitude. Method 2 used the final V_a and B from the model was used as a start point for the calculation. A linear relationship was assumed to change the B value with altitude, raising the magnetic field by 500 nT every 250 km, starting at $3.6 R_e$, resulting in magnetic field value of 53,000 nT at 100 km, as gathered from IGRF (*Finlay et al.* [2010]). Method 2 added .12 seconds to the times listed in Table 9.

Method 3 included both Method 1 and 2 variable estimations; 100% O^+ levels from 2,500 km to 100 km, and a changing B at the rate of 500 nT per 250 km from $3.6 R_e$ to 100 km, the travel time would add an additional .15 seconds to the previous listed times in

Method	Alt _{start}	Alt _{end}	Assumption	t [sec]
1	3.6 R _e	2500 km	Used V _a at 3.6R _e	1.15
1	2500 km	100 km	Used 100% O ⁺ density	0.54
2	3.6 R _e	100 km	Changing B with altitude	.12
3	3.6 R _e	2500 km	Changing B with altitude and 100% O ⁺ density from 2500-100 km	.13

Table 10. Additional time travel based on different assumptions made at given altitudes. Method 3 was the chosen method as it is the most accurate.

Table 8 if added. Since the ground and satellite data being used to look for signatures does not have this great of a resolution, the additional .15 seconds was neglected.

3.4. Size of Ionospheric Vorticies

Local MHD simulations were ran to determine the size of the KHI vorticies in the ionosphere for the events listed in Table 1. This research follows similar steps as described by *Nykyri* [2003]. Resistive MHD equations (*Otto* [1990]) are used in the simulations and are solved using the finite difference leap frog scheme (*Potter* [1973]). Initial conditions were gathered from the Cluster data and normalized to the simulation units. Our basis for determining the ionospheric vorticity size is determined by the conservation of magnetic flux. The formula used to determine the area of the ionospheric vorticity is a ratio of the ionospheric and magnetospheric magnetic fields, as given below:

$$A_I = A_M \frac{B_M}{B_I}$$

where B_M is the magnetospheric magnetic field, B_I is the ionospheric magnetic field, and A_M and A_I are the magnetospheric and ionospheric vortex areas. B_M is calculated by using the average value of B_{msp} and B_{msh} and B_I is determined from International Geomagnetic Reference Field version 11.0 (*Finlay et al.* [2010]). To calculate A_M , the vortex dimensions are determined from the simulation output corresponding to the time when the plasma fluid elements form a full vortex. When A_I is calculated, new vorticity dimensions for the ionospheric vorticity are approximated.

Table 11 shows the final results of our research, the approximated dimensions of the vorticity at 100 km in the ionosphere. These dimensions are consistent with previously published sighting of auroral bright spots which were deemed an effect of a KHI vorticity. *Lui* [1989] measured auroral bright spots in his paper with

dimensions of 50-200 km and *Farrugia et al.* [1994] measured his auroral bright spot event with dimensions of 40-100 km. NASA's Polar Ultraviolet Imager, orbiting approximately at 3 R_e, has an angular resolution of 0.036 degrees (*Marshall Space Flight Center*), yielding a spatial resolution of about 11 km. IMAGE Far Ultraviolet Imager has a spatial resolution of about 150 km (*Bisikalo et al.* [2003]).

Convection vorticies are another ionospheric phenomena which are produce by KHI signatures and reconnection. The Super Dual Auroral Radar Network (SuperDARN) has a resolution of about 45 km (*Greenwald et al.* [1995]), however it's reflection region is in the F-region, at altitudes from 150-800 km. As the magnetic field is significantly different at these altitudes compared to 100 km, new dimensions need to be calculated for the vortex. The ratio between the magnetic field values at the 100 km over the 600 km value was approximately 1.3 for all cases at both poles. Therefore the area of the vorticity would increase by 30% at 600 km when compared to 100 km. As the area for an ellipse is $A = \pi xy$, it would be a simple assumption increase the vortex dimensions listed in Table 11 by 15%. This would roughly conserve the ratio of x and y dimensions and total area as done when calculating the dimensions in Table 11. Since the vortex in the F-region would be larger than at 100 km, SuperDARN's resolution would be more than sufficient to resolve the vortex in this region.

4. Discussion and Conclusion

The purpose of this research was to determine an ionospheric location to look for potential ionospheric signatures of KHI events. The time for the perturbation to travel from its magnetospheric location to the ionosphere was calculated so the correct satellite and ground data could be looked at. Finally, the area of the vortex observed at 100km and 600km in the ionosphere was determined, so depending on which instrument is

Event	X_M [R_e]	Y_M [R_e]	X_I [km]	Y_I [km]	X_I [km]	Y_I [km]
			North	North	South	South
1	1.88	1.26	246	158	250	160
2	0.942	0.542	-	-	122	70
3	1.41	0.989	-	-	215	150
4	0.895	0.848	110	103	-	-
5	0.848	0.753	100	85	106	94
6	1.32	1.13	142	122	150	131
7	0.989	0.848	79	68	77	67

Table 11. Approximate vorticity dimensions at 100 km for the magnetosphere and northern/southern ionosphere (Finlay et al. [2010])

looked at, the proper dimensions could be looked for. the next step is to gather the satellite and ground data and look at the projected times in the calculated geomagnetic locations for a signature of the determined dimensions. We plan to look at auroral satellite data, ground radar, magnetometer, and optical data for potential signatures. As potential signatures have already been observed by optical (Farrugia et al. [1994]) and auroral data (Lui [1989]), we have an idea of what signatures should be present. We expect to see convection vortices at the determined geomagnetic locations in the radar data and magnetic variations in the ground magnetometer data. Once signatures have been found, our goal is to reverse engineer the process to locate a KHI event; we will use the ionospheric signatures to determine if, when, and where a KHI has taken place in the magnetosphere. This will be an asset to the entire scientific community, as current satellite coverage is too minimal to cover the vast magnetospheric area needed to observe all the KHI event which are taking place.

Acknowledgments

Simulation results have been provided by the Community Coordinated Modeling Center at Goddard Space Flight Center through their public Runs on Request system (<http://ccmc.gsfc.nasa.gov>). The CCMC is a multi-agency partnership between NASA, AFMC, AFOSR, AFRL, AFWA, NOAA, NSF and ONR. The OpenGGCM Model was developed by Joachim Raeder, Timothy Fuller-Rowell at the University of Michigan. The BATS-R-US Model was developed by Dr. Tamas Gombosi et al. at the University of New Hampshire.

References

- Bilitza, International reference ionosphere 2000, *Radio Science* 36, 2, 261–275, 2001.
- Bisikalo et al., Remote sensing of the proton aurora characteristics from image-fuv, *Annales Geophysicae*, 21, 2165–2173, 2003.
- Chandrasekhar, S., *Hydrodynamic and Hydromagnetic Stability*, Clarendon Press, 1961.
- Deehr et al., Influence of the ionosphere on the altitude of discrete auroral arcs, *Annales Geophysicae*, 23, 1–8, 2005.
- Fairfield et al., Geotail observations of the kelvin-helmholtz instability at the equatorial magnetotail boundary for parallel northward fields., *J. Geophysical Research*, 2000.
- Farrugia et al., Auroral activity associated with kelvin-helmholtz instability at the inner edge of the low-latitude boundary layer, *Journal of Geophysical Research*, 99, 19,403–19,411, 1994.
- Finlay et al., International geomagnetic reference field: the eleventh generation. international association of geomagnetism and aeronomy, working group v-mod., *Geophys. J. Int.*, 183, 1216–1230, 2010.
- Greenwald et al., A global view of the dynamics of high-latitude convection, *Space Science Reviews*, 71, 761–796, 1995.
- Hasegawa et al., Transport of solar wind into earth’s magnetosphere through rolled-up kelvin-helmholtz vortices, *Nature*, 430, 755–758, 2004.
- Lui, A. T. Y., Auroral bright spots on the dayside oval, *Journal of Geophysical Research*, 94, 5515–5522, 1989.
- Marshall Space Flight Center, Instrument description. NASA:CCMC, C. C. M. C., Model’s at a glance.

- Nykyri, Influence of the kelvin-helmholtz instability on the plasma transport at the magnetospheric boundary, Ph.D. thesis, University of Alaska Fairbanks, 2003.
- Nykyri et al., Cluster observations of reconnection due to the kelvin-helmholtz instability at the dawn-side magnetospheric flank, *Annales Geophysicae*, *24*, 2619–2643, 2006.
- Nykyri et al. [2001], Plasma transport at the magnetospheric boundary due to reconnection in kelvin-helmholtz vortices, *Geophysical Research*.
- Otto, 3d resistive mhd computations of megnetospheric physics, *Computational Physics Communications*, 1990.
- Otto et al., Kelvin-helmholtz instability at the magnetotail boundary: Mhd simulation and comparison with geotail observations, *J. Geophysical Research*, *105*, 2000.
- Potter, *Computational Physics*, John Wiley, 1973.

E Hyatt, Department of Engineering Physics, Embry-Riddle Aeronautical University, Daytona Beach, FL 32114. (e-mail: Dougale@my.erau.edu)

This preprint was prepared with AGU's L^AT_EX macros v5.01, with the extension package 'AGU++' by P. W. Daly, version 1.6b from 1999/08/19.